Mechanism and stability of an Fe-based 2D MOF during the photoelectro-Fenton treatment of organic micropollutants under UVA and visible light irradiation

Zhihong Ye [1,2], Giulia E.M. Schukraft [2], Anouk L´Hermitte [2], Ying Xiong [2], Enric Brillas [1], Camille Petit [2,**], Ignasi Sirés [1,*]

[1] *Laboratori d'Electroquímica dels Materials i del Medi Ambient, Departament de Química Física, Facultat de Química, Universitat de Barcelona, Martí i Franquès 1-11, 08028 Barcelona, Spain*

[2] *Barrer Centre, Department of Chemical Engineering, Imperial College London, South Kensington Campus, London SW7 2AZ, UK*

* Corresponding author: i.sires@ub.edu (I. Sirés)

** Corresponding author: camille.petit@imperial.ac.uk (C. Petit)

Abstract

This work reports the novel application of an Fe-based 2D metal−organic framework (MOF), prepared with 2,2'-bipyridine-5,5'-dicarboxylate (bpydc) as organic linker, as highly active catalyst for heterogeneous photoelectro-Fenton (PEF) treatment of the lipid regulator bezafibrate in a model matrix and urban wastewater. Well-dispersed 2D structures were successfully synthesized and their morphological, physicochemical and photocatalytic properties were assessed. UV/Vis PEF using an IrO_2/air-diffusion cell with an extremely low catalyst concentration (0.05 g L^{-1}, tenfold lower than reported 3D MOFs) outperformed electro-oxidation with electrogenerated H_2O_2, electro-Fenton and visible-light PEF. Its excellent performance was explained by: (i) the enhanced mass transport of H_2O_2 (and organic molecules) at the 2D structure, providing active sites for heterogeneous Fenton's reaction and in-situ Fe(II) regeneration; (ii) the ability of photoinduced electrons to reduce H_2O_2 to $^{\bullet}OH$, and Fe(III) to Fe(II); and (iii) the enhanced charge transfer and excitation of Fe−O clusters, which increased the number of electron-hole pairs. LC-QToF-MS and GC-MS allowed the identification of 16 aromatic products of bezafibrate. The complete removal of four micropollutants mixed in urban wastewater at pH 7.4 revealed the great potential of (Fe−bpydc)-catalyzed PEF process.

Keywords: Fe−bpydc; Heterogeneous photoelectro-Fenton; Metal−organic framework Pharmaceutical; Water treatment

1. Introduction

Electrochemical advanced oxidation processes (EAOPs) comprise technologies with strong growth prospects for the treatment of persistent organic micropollutants in water (Martínez-Huitle et al., 2015; Cornejo et al., 2020), and can become self-sustainable when combined with renewable energy sources (Mook et al., 2014). Among these processes, electro-Fenton (EF) process dominates, showing a great effectiveness derived from the production of free hydroxyl radical ($^{\bullet}OH$) via Fenton's reaction (1) (Brillas et al., 2009; Zhou et al., 2018). In EF, H_2O_2 is electrogenerated on site from O_2 reduction reaction (2) (Zhou et al., 2019), with the air-diffusion cathode the best choice to ensure the highest reduction rate at ambient conditions (Barazesh et al., 2015; Lanzalaco et al., 2017; Pérez et al., 2018; Alcaide et al., 2020; Zhang et al., 2020). In undivided cells, hydroxyl radicals adsorbed on the anode (M) surface via reaction (3) (Klidi et al., 2018) also contribute to oxidation (Salmerón et al., 2019; Yang et al., 2019). Photoelectro-Fenton (PEF) is an upgraded EF process in which the solution is exposed to irradiation with UVA or sunlight (Flores et al., 2017). UV photons can photoreduce Fe(III), either complexed with a carboxylated organic ($R{-}COO^-$) via reaction (4) or in its hydrated form via photo-Fenton reaction (5), thus promoting the continuous Fe^{2+} regeneration (Steter et al., 2018; Zhou et al., 2018; Tao et al., 2019).

$$Fe^{2+} + H_2O_2 \rightarrow Fe^{3+} + {}^{\bullet}OH + OH^- \quad (1)$$

$$O_2(g) + 2\,H^+ + 2\,e^- \rightarrow H_2O_2 \quad (2)$$

$$M + H_2O \rightarrow M(^{\bullet}OH) + H^+ + e^- \quad (3)$$

$$Fe(OOCR)^{2+} + h\nu \rightarrow Fe^{2+} + CO_2 + R^{\bullet} \quad (4)$$

$$[Fe(OH)]^{2+} + h\nu \rightarrow Fe^{2+} + {}^{\bullet}OH \quad (5)$$

Practical constraints challenge the implementation of conventional EF and PEF at industrial scale (Zhou et al., 2018; Bello et al., 2019). Specifically, there is a need for catalysts that can replace the hydrated Fe^{2+} in reaction (1). This is due to the fact Fe^{2+} is unstable at the circumneutral pH of many water effluents. Aiming to minimize the iron precipitation, which is detrimental due to the loss of catalytic power and the accumulation of sludge (Hinojosa Guerra et al., 2019), two main approaches have been suggested: (i) the addition of complexing agents, like ethylenediamine-*N,N'*-disuccinic (EDDS) acid, to stabilize Fe(III) as a soluble catalyst that can still makes homogeneous Fenton's reaction viable at near-neutral pH (Hinojosa Guerra et al., 2019; Tao et al., 2019; Ye et al., 2019, 2020a); and (ii) the use of heterogeneous catalysts, which allow the H_2O_2 decomposition on their surface to yield $^{\bullet}OH$ and can also yield dissolved Fe^{2+} (Ganiyu et al., 2018; Poza-Nogueiras et al., 2018). Although several synthetic structures have been proposed as iron-based heterogeneous catalysts in EF (Ganiyu et al., 2018; Zhou et al., 2018), iron oxide (Ltaïef et al., 2018; dos Santos et al., 2020) and sulfide (Labiadh et al., 2015; Barhoumi et al., 2016; Ltaïef et al., 2018) minerals seem a more sustainable alternative. However, the properties of these minerals may vary significantly depending on the source, and they tend to undergo excessive iron leaching or show sluggish kinetics for Fe(III) reduction, (Ye et al., 2020b).

Recently, increasing attention has been paid to metal−organic frameworks (MOFs) as highly porous materials, well suited for water treatment due to their large surface area and open metal sites (Dias and Petit, 2015; Silva et al., 2015; Li et al., 2019; Sharma and Feng, 2019). The Fe-

74 MOFs are especially interesting as catalysts in Fenton-based AOPs due to the Fe(III)/Fe(II)
75 interconversion and presence of photosensitive Fe−O clusters (Sharma and Feng, 2019). Several
76 3D Fe-based MOFs have been synthesized over the last five years, and their ability to catalyze
77 the degradation of organic pollutants in heterogeneous Fenton and photo-Fenton systems has
78 been discussed (Gao et al., 2017; Tang and Wang, 2018). In contrast, the application of 3D Fe-
79 based MOFs in EF and PEF has been rarely reported. Within this context, two main strategies
80 have been followed: (i) preparation of MOF-based Fe/C cathodes (Le et al., 2016; Zhao et al.,
81 2017; Liu et al., 2019; Lu et al., 2020) and (ii) addition as suspended heterogeneous catalysts (Ye
82 et al., 2020b, 2020c). In both cases, the MOFs are typically pyrolyzed to confer them enough
83 stability.

84 Lately, 2D MOFs are presumed to exhibit an enhanced activity because their active sites are
85 more accessible (Dhakshinamoorthy et al., 2019). The diffusion barrier for molecules becomes
86 smaller, which favors their potential application to catalysis (Bai et al., 2019). 2D morphologies
87 are varied, including porous crystals with a high lateral-to-thickness aspect ratio
88 (Dhakshinamoorthy et al., 2019). To our knowledge, the use of 2D Fe-MOFs as heterogeneous
89 catalysts in EF or PEF has never been reported, and only a small number of them or their
90 derivatives has been tested in Fenton and photo-Fenton processes (Li et al., 2016, 2018; Hou et
91 al., 2019). Using 2,2'-bipyridine-5,5'-dicarboxylate (bpydc) as linker, the resulting Fe−bpydc
92 may exhibit high catalytic activity for H_2O_2 activation at circumneutral pH (Li et al., 2016).

93 This article proposes, for the first time, the use of a very low amount of an Fe−bpydc 2D
94 MOF as heterogeneous PEF catalyst under illumination with UV or visible light. The electronic

95 structure of the catalyst and the performance of the heterogeneous PEF treatment of bezafibrate
96 solutions were thoroughly evaluated. Bezafibrate is a massively prescribed fibrate drug that
97 regulates cholesterol and triglycerides (Yin et al., 2020). Since it is hardly removed by
98 conventional wastewater treatment, it has been detected in municipal facilities and natural water
99 at concentrations up to 4.6 μg L^{-1} (Sui et al., 2017), seriously jeopardizing human health and
100 ecosystems (Rivas et al., 2019; Solís et al., 2019).

101 Bezafibrate solutions in model matrices and urban wastewater at natural pH have been
102 treated by the (Fe−bpydc)-catalyzed PEF system using an IrO_2/air-diffusion cell. Initial pH,
103 applied current and catalyst dosage were optimized from bezafibrate concentration decay. The
104 oxidation products were detected by gas chromatography-mass spectrometry (GC-MS) and
105 liquid chromatography quadrupole time-of-flight mass spectrometry (LC-QToF-MS) to elucidate
106 the degradation routes. The physicochemical properties, electronic structure, stability and
107 recyclability of Fe−bpydc were studied by various techniques, and a mechanism for the
108 heterogeneous PEF treatment of bezafibrate is proposed.

109 **2. Experimental**

110 *2.1. Chemicals*

111 Bezafibrate (≥ 98% purity) was purchased from Sigma-Aldrich. Sodium sulfate,
112 concentrated sulfuric acid and sodium hydroxide pellets were of analytical grade from Merck.
113 $Fe(ClO_4)_2$ and dimethylformamide (DMF) from Sigma-Aldrich, as well as bpydc from TCI
114 Chemicals, all of analytical grade, were employed for the Fe−bpydc synthesis. Analytical grade

115 $TiOSO_4$ and 5,5-dimethyl-1-pyrroline-N-oxide (DMPO), both from Sigma-Aldrich, were used
116 for H_2O_2 determination and electron spin resonance (ESR) analysis, respectively. All the other
117 chemicals were of analytical or HPLC grade acquired from Merck and Panreac. All synthetic
118 solutions were prepared with Milli-Q water from Merck Millipore, whereas urban wastewater
119 employed in some trials was collected from a municipal facility (Text S1).

120 *2.2. Catalyst synthesis*

121 Fe−bpydc was prepared in a glass container upon modification of a reported procedure (Li
122 et al., 2016). Briefly, 0.5 mmol of bpydc were dissolved in 40 mL DMF, and the resulting solution
123 was added to 40 mL of an aqueous solution containing 1 mmol of $Fe(ClO_4)_2$. The mixture was
124 sonicated for 20 min to ensure homogeneity, and subsequently heated in an oil bath at 120 ºC for
125 4 h under vigorous stirring. Once cooled down, the red-brown solid product was separated by
126 filtration, washed exhaustively with ethanol and dried overnight at 60 °C.

127 *2.3. Catalyst characterization*

128 The morphological features of the synthesized Fe−bpydc were observed by field-emission
129 scanning electron microscopy (FESEM) employing a JEOL JSM7001F microscope. Powder X-
130 ray diffraction (XRD) analysis was conducted using a PANalytical X'Pert PRO MPD Alpha-1
131 diffractometer, using Cu $K_{\alpha 1}$ radiation ($\lambda = 1.54178$ Å) and operating at 40 kV and 20 mA within
132 the range of 5-50°. X-ray photoelectron spectroscopy (XPS) was performed in an ultrahigh
133 vacuum spectrometer (see information in Text S2). Thermogravimetric analysis (TGA) was
134 carried out with a Netzsch TG 209 F1 Libra instrument between 20 and 900 ºC at a heating rate
135 of 10 ºC min^{-1} under N_2 atmosphere; the temperature was maintained at 120 ºC for 40 min.

Nitrogen adsorption and desorption isotherms were acquired using a Micrometrics 3Flex sorption analyzer at -196 ºC. Prior to analysis, the samples were degassed by heating the samples at ~0.2 mbar for 5 h at 90 °C to remove the majority of the residual solvent and degassed in situ on the porosity analyzer at ~0.003 mbar. The surface area was calculated using the Brunauer–Emmett–Teller method (Brunauer et al., 1938). The total pore volume was calculated from the N_2 adsorption at a relative pressure (P/P_0) of 0.993.

DR-UV/Vis spectroscopy was carried out using an Agilent Cary 500 UV–Vis-NIR spectrometer equipped with an integrating sphere. Attenuated total reflection Fourier transform-infrared (FT-IR) spectra were collected using an Agilent Technologies Cary 630 FTIR at room temperature. To obtain the ESR spectra DMPO was used as spin trap (see description in Text S3).

2.4. Electrochemical systems

The electrolyses were performed in a single-compartment glass cell containing 150 mL of solution, thermostated at 25 ºC and placed over a magnetic stirrer to ensure a high mass transport. The anode was either a 3 cm^2 dimensionally stable metal oxide (i.e., IrO_2-based or Ru_2O-based) on a Ti plate, purchased from NMT Electrodes, or a 3 cm^2 boron-doped diamond (BDD) thin film on Si, supplied by NeoCoat. The cathode was a 3 cm^2 commercial carbon-polytetrafluoroethylene (PTFE) cloth from BASF, mounted as reported before (Steter et al., 2018) and fed with air at 1 L min^{-1}. The interelectrode gap was close to 1.0 cm. A preliminary polarization of all the electrodes in a 0.050 M Na_2SO_4 solution at 300 mA for 180 min allowed the stabilization of their active surfaces. In photo-assisted trials, the solution was irradiated with a Xe arc lamp (150 or 300 W, $\lambda > 325$ nm) purchased from LOT Quantum Design, which emitted

light from 5 cm above the liquid surface. UV/Vis trials were made without light filter, whereas a UV filter (400FH90-50S) with a cut-off value of 400 nm was inserted to study visible-light PEF.

2.5. Analytical procedures

The electrical conductance of the raw urban wastewater was measured with a Metrohm 914 conductometer, which also determined the solution pH. The samples were always filtered to remove microparticles. The concentration of H_2O_2 produced from reaction (2) was determined by the colorimetric titanate method (Welcher, 1975) using a Shimadzu 1800 UV/Vis spectrophotometer, at λ = 408 nm and 25 °C. The concentration of cations was determined by inductively coupled plasma optical emission spectroscopy (ICP-OES) in a Perkin Elmer Optima 3200L spectrometer. The TOC content of samples before and after degradation was measured upon withdrawal, injecting them in a Shimadzu TOC-VCSN analyzer that yielded values with ±1% accuracy.

Bezafibrate concentration was measured by reversed-phase HPLC in a chromatograph equipped with a Luna C18 3 μm, 100 mm × 4.6 mm, column at 30 °C and an SPD-20A detector set at 210 nm. A 40:55:5 (v/v/v) mixture containing acetonitrile, acetic acid in water (0.02 vol.%) and methanol was used as the mobile phase, eluted at 1.0 mL min^{-1}, yielding a peak at 6.8 min.

The organic products accumulated during selected treatments of bezafibrate were identified by GC-MS and LC-QToF-MS, as described in Supplementary Material file (Text S4).

3. Results and discussion

3.1. Characterization of Fe−bpydc catalyst

177 The morphological characteristics of the as-synthesized catalyst were revealed by FESEM
178 analysis. Fig. 1a and 1b display 2D irregular-shaped plates with size up to tens of microns,
179 whereas their thickness ranged from hundreds of nanometers to few microns (Fig. 1b). The
180 asymmetric lateral and vertical expansion of the 2D sheets concomitantly induces the formation
181 of more accessible active sites, thereby decreasing the diffusion barrier (Kondo et al., 2006). The
182 XRD pattern depicted in Fig. 1c confirms the high crystallinity of the Fe−bpydc MOF structure,
183 in good agreement with the simulated one calculated from CIF file using Mercury software (Finn
184 and Zubieta, 2002; Li et al., 2016), which confirms the successful catalyst preparation. The
185 poorly defined reflection appearing at 35.7º was related to the typical peak of iron oxides like
186 Fe_3O_4 (JCPDS 89-0596), whose presence is explained by the surface oxidation occurring during
187 the synthesis, although its contribution seems quite small. As can be seen in Fig. 1d, the
188 asymmetric unit of Fe−bpydc involves one iron atom, one bpydc ligand, one coordinated and one
189 lattice water molecules. The six-coordinate geometry of central iron is defined by the two oxygen
190 donors of the η^2-carboxylate of a bpydc ligand, one oxygen of the η^1-carboxylate of a second
191 bpydc ligand, two nitrogen donors of a third chelating bpydc ligand and one oxygen of the
192 terminal H_2O ligand (Finn and Zubieta, 2002). The carboxylate groups and N atoms of the bpydc
193 ligands bridge alternately the successive iron centers to yield a layered 2D metal−organic
194 network, whereas the pendant H_2O ligands directed toward the interlamellar region can be
195 connected to the carboxylate groups through hydrogen bonds, providing further extension of the
196 2D plates (Finn and Zubieta, 2002). The empirical formula of Fe−bpydc can then be proposed as
197 $[Fe(C_{12}H_8N_2O_4)(H_2O)]\cdot H_2O$, with a molecular weight of 334 g mol^{-1}. The TGA curve of this

material, shown in Fig. 1e, reveals a mass loss of ~10% during the constant heating at 120 °C, corresponding to the elimination of the coordinated and lattice water (in very good agreement with 10.7% calculated from the empirical formula). The dehydrated sample remained stable up to ~500 °C. On the other hand, the TGA curve of bpydc revealed that the organic linker alone was only stable up to ~300 °C, thus gaining stability upon coordination.

The surface composition of Fe−bpydc was analyzed by XPS. Fig. S1 highlights the presence of C, O, N and Fe elements. In the high resolution Fe 2*p* XPS spectrum of Fig. 2a, the deconvolution of the Fe $2p_{3/2}$ and Fe $2p_{1/2}$ bands informed about the existence of two peaks in each one. The fitting peaks centered at 710.8 and 724.1 eV corresponded to Fe(II), whereas those appearing at 714.0 and 726.8 eV were assigned to Fe(III) (Ye et al., 2020c). The existence of Fe(III) is consistent with the XRD results. The high resolution spectrum of N 1*s* in Fig. 2b clearly shows a single peak at 400.0 eV, corresponding to pyridinic N (Ye et al., 2020b), in agreement with the structure of the as-synthesized Fe−bpydc (Fig. 1d). N-doping is another interesting feature of the synthesized catalyst, since it is expected to enhance the electron transfer and catalytic activity (Yang et al., 2019). The specific surface area and the pore structure of the Fe−bpydc samples were determined using N_2 adsorption−desorption measurements, which are depicted in Fig. S2. As can be seen, the Fe−bpydc particles exhibited Type II isotherm with almost no hysteresis loop, which can be associated to the presence of macropores in the structure (Thommes et al., 2015). The specific BET surface area and total pore volume of the as-prepared Fe−bpydc were 15 $m^2\ g^{-1}$ and 0.036 $cm^3\ g^{-1}$, respectively.

3.2. Catalytic properties of Fe−bpydc

Fig. 3a shows the degradation of bezafibrate at a concentration of 0.044 mM (10 mg C L^{-1}) in 0.050 M Na_2SO_4 solutions at natural pH ~ 5.1 upon the application of different treatments. The presence of 0.05 g L^{-1} Fe−bpydc as suspended particles in the bezafibrate solution yielded a drug removal of 5%, which informed about its negligible adsorption capacity. Similarly, the concentration decay was also poor (7%) under UV/Vis photocatalysis. This result suggests that the photogenerated holes were not strong enough to directly oxidize bezafibrate, and the valence band (VB) position of Fe−bpydc cannot reach the oxidation potential of the $H_2O/^{\bullet}OH$ pair (see subsection 3.5), thus impeding the formation of $^{\bullet}OH$ from photoinduced water oxidation. In addition, this result informs about the stability of bezafibrate to direct UV/Vis photolysis. A small drug abatement of 27% was attained after 90 min of electro-oxidation with electrogenerated H_2O_2 (EO-H_2O_2, without Fe−bpydc), as expected from the mild oxidation caused by H_2O_2 and $IrO_2(^{\bullet}OH)$ generated from reactions (2) and (3), respectively (Martínez-Huitle et al., 2015). In contrast, heterogeneous EF catalyzed with 0.05 g L^{-1} Fe−bpydc achieved a more substantial removal of 42% at 90 min thanks to the formation of $^{\bullet}OH$ from Fenton's reaction, confirming the catalytic activity of Fe−bpydc. The degradation in visible-light PEF was clearly superior, reaching 55% removal in 90 min. This proves that Fe−bpydc can act as a visible-light photocatalyst due to the direct excitation of the Fe−O cluster. The photogenerated electrons may contribute decisively in the reduction of Fe(III) (Cheng et al., 2018). Yet, the fast electron-hole recombination rate on the photocatalyst limited the bezafibrate removal. When the UV/Vis PEF process was applied, the drug degradation was significantly improved and outperformed all the other treatments, showing a drug disappearance of 92% in 90 min. The presumably high

absorbance of Fe−bpydc within the UV region can explain this result, as it promotes the generation of electron/hole pairs and the Fe(III) photoreduction. In conventional homogeneous PEF, the photochemically active range is quite restricted to the UVA region with λ_{max} = 365 nm (Flores et al., 2017), since these photons are able to promote/stimulate reactions (4) and (5) in solution (Zhou et al., 2018). The introduction of Fe−bpydc as heterogeneous PEF catalyst allows the utilization of a wider wavelength range, including visible light and hence, the synergistic contribution of photocatalysis and heterogeneous Fenton and photo-Fenton reactions accelerated the formation of radicals like •OH that effectively degraded bezafibrate.

Fig. S3 highlights the gradual H_2O_2 accumulation up to 14.8 mM at 90 min via reaction (2) in EO-H_2O_2, which decreased to 10.8 mM in Fe−bpydc catalyzed EF due to its partial destruction from Fenton's reaction (1). This content decreased down to 8.0 mM under UV/Vis illumination in (Fe−bpydc)-catalyzed PEF, mainly because the photogenerated charge carriers accelerated the Fe(II) regeneration and the subsequent H_2O_2 decomposition. Under the latter conditions, the partial H_2O_2 reduction and oxidation promoted by the electrons and holes, respectively, cannot be discarded either (see subsection 3.5).

The effect of light intensity was further investigated, by comparing the previous results (150 W lamp) with those obtained using a 300 W Xe arc lamps. Fig. 3b shows that the visible-light PEF with the higher power lamp yielded 87% drug decay, being clearly superior to the previous performance. This confirmed the promising visible-light photocatalytic activity of Fe−bpydc. In addition, a much faster and complete drug degradation can be observed in UV/Vis PEF with the 300 W lamp. The larger number of photons reaching the suspension per unit area as the light

intensity was increased can explain this observation. The UV/Vis irradiation then showed a remarkable superiority as compared to visible light in the (Fe−bpydc)-catalyzed PEF, providing a greater photon energy that enhanced the charge transfer and promoted the Fe(III)/Fe(II) cycling (Zhao et al., 2017). However, the treatment of bezafibrate solutions at 300 W would likely entail a higher operation cost. For this reason, subsequent studies were conducted under UV/Vis light irradiation with the 150 W lamp.

The effects of initial pH, applied current, catalyst dosage, anode type and electrolyte on the normalized bezafibrate concentration decay upon the application of heterogeneous UV/Vis PEF treatment with Fe−bpydc are shown in Fig. 4a-e. As observed in Fig. 4a, the degradation efficiency of bezafibrate was enhanced at more acidic initial pH, although the continuous disappearance was feasible within all the pH range 3.0-9.0. Overall removal was achieved in 90 min at initial pH 3.0, the optimal value for Fenton's reaction (1) (Zhu et al., 2018), gradually decreasing down to 58% at pH 9.0. This loss of performance can be ascribed to the decrease of the oxidation potential of $^{\bullet}OH$, which changed from ~2.7 to 1.9 V when pH increased from 3.0 to 7.0 (Zhu et al., 2018). Furthermore, the leaching and dissolution of iron ions becomes more difficult at higher pH, reducing the contribution of homogeneous Fenton's reaction. It should be stressed that 92% and 82% drug removal could be still achieved at 90 min at initial pH 5.1 and 7.0, respectively, corroborating the high catalytic activity at circumneutral pH.

Fig. 4b shows the decrease of solution pH in all cases, owing to the generation of acidic products like carboxylic acids (Flores et al., 2017; Steter et al., 2018). The slightly higher dissolved iron concentration at initial pH 3.0 is also evidenced, which promoted the occurrence

of homogeneous reaction (1). However, the reusability under such apparently good conditions might decrease because of the larger decomposition of Fe−bpyc.

Current increase had a positive influence, as deduced from Fig. 4c. This observation was more evident when moving from 50 to 150 mA, giving rise to a greater H_2O_2 electrogeneration and the consequently higher •OH concentration. As expected, Fig. 4d highlights that a larger amount of catalyst from 0.0125 to 0.075 g L^{-1} allowed a substantial rise in the degradation efficiency, from 58% to 96%. A larger number of Fe−bpydc particles means a greater amount of available active sites, favoring the interactions with the pollutant and H_2O_2 molecules, as well as the incidence of more photons on photocatalyst surface. However, the enhancement of bezafibrate decay after 90 min when comparing the trials with 0.05 and 0.075 g L^{-1} catalyst was not significant, probably because of the parasitic reaction between •OH and the excess of Fe(III) and Fe(II). Therefore, the optimum content was 0.05 g L^{-1}, i.e., 10- to 20-fold lower than that reported using 3D MOF-catalyzed Fenton (Tang and Wang, 2018) and EF (Ye et al., 2020b, 2020c) systems. This means that the unique 2D structure of Fe−bpydc provided a more efficient mass transport (Bai et al., 2019). This is very interesting from an application standpoint, since a low catalyst dosage is preferred because of the lower operation cost, easier recovery, smaller amount of sludge and better light penetration.

Fig. 4e clarifies the importance of the electrolyte composition. The degradation profile using the IrO_2 anode in a 0.041 M Na_2SO_4 + 0.009 M $NaHCO_3$ mixture at natural pH ~ 8.0 was much slower than in Na_2SO_4, achieving only 39% abatement at 90 min. This can be attributed to the scavenging role of CO_3^{2-} and HCO_3^- ions via reactions (6) and (7) with k_2 values of 4.0×10^8 and

303 8.5×10^6 M^{-1} s^{-1}, respectively (Ye et al., 2020a). When BDD replaced the IrO_2 anode in the
304 bezafibrate solution with 0.050 M Na_2SO_4, the decay profile was exactly the same. This confirms
305 that the dominant species responsible for the drug abatement was $^{\bullet}OH$ generated in the bulk via
306 Fenton's reaction (1), rather than adsorbed M($^{\bullet}OH$). Conversely, the trial with a RuO_2 anode in
307 0.025 M Na_2SO_4 + 0.035 M NaCl yielded the quickest decay, owing to partial oxidation by active
308 chlorine generated at the M surface, without discarding the action of $Cl^{\bullet}$ formed via reaction (8)
309 (Zhu et al., 2018).

310 $$^{\bullet}OH + CO_3^{2-} \rightarrow CO_3^{\bullet-} + OH^- \quad (6)$$

311 $$^{\bullet}OH + HCO_3^- \rightarrow CO_3^{\bullet-} + H_2O \quad (7)$$

312 $$HClO + h\nu \rightarrow {}^{\bullet}OH + Cl^{\bullet} \quad (8)$$

313 *3.3. Stability and reusability of Fe−bpydc*

314 A critical issue for the practical application of raw MOFs is, for some of them, their excessive
315 lack of stability in water (Liu et al., 2018). The metal nodes may react, displacing ligands and
316 causing phase changes, loss in crystallinity and decomposition, eventually destroying the porous
317 structure (Taylor et al., 2012). Nevertheless, the decomposition of MOFs in water has been
318 scarcely studied during water treatment. The oxidative resistance of the pyridine ring to $^{\bullet}OH$
319 attack and its strong binding affinity with Fe(II) ion are key reasons for using bipyridine as ligand.
320 The introduction of carboxylic groups to the 2,2´-bipyridine ligand can stabilize the final
321 products, because the carboxyl group binds to Fe(III) ion in the catalytic cycle, thus minimizing
322 its hydrolysis (Cheng et al., 2018). The reusability of Fe−bpydc was evaluated from successive
323 bezafibrate degradation runs. Fig. 5a shows a small but progressive performance loss, of 30% as

maximal, after three runs of 90 min. The turnover frequency (TOF) to evaluate the catalytic efficiency of the active sites was calculated as follows (Li et al., 2019):

$$TOF = \frac{n_p}{n_c\, t} \quad (9)$$

where n_p is the number of moles of pollutants removed, n_c is the number of moles of catalyst and t is the reaction time (h). The TOF value after the third run was 0.161 h^{-1}, outperforming the values reported for some MOFs like MIL(Fe)-101 for Fenton treatment (Lv et al., 2015). This proves the high catalytic activity of Fe−bpydc, although the decrease in removal rate suggests a certain degree of deactivation in water, which merits to be assessed.

The used catalyst was characterized to evaluate the chemical and structural changes. The XRD patterns (Fig. 5b) and FTIR spectra (Fig. S4), corresponding to fresh and used Fe−bpydc, show that the crystallinity and chemical structure remained quite stable along the treatment, without any evidence of alteration. Based on this, partial amorphisation of some of the MOF particles cannot be discarded, but it seems that the catalyst deactivation could be rather related to the blockage of some of its active sites by intermediates, as suggested elsewhere (Li et al., 2016). The greater exposure of active sites derived from the open 2D structure leads to more significant blockage risk.

The assessment of the stability of Fe−bpydc in water was conducted by dosing 0.05 g L^{-1} of catalyst to 150 mL of ultrapure water. The dissolved iron and TOC release vs time at different initial pH values are displayed in Fig 5c and d. A much faster decomposition of Fe−bpydc can be observed at initial pH 3.0, reaching 1.5 mg L^{-1} iron leaching (~18 wt.%) and 4.2 mg L^{-1} TOC dissolution in 90 min. These results agree with the expected intolerance of Fe−bpydc to acidic

345 conditions because of the iron dissolution, which justifies the greater dissolved iron concentration
346 value in Fig. 4b. Conversely, only ~0.8 mg L^{-1} iron (~9 wt.%) were leached when pH increased
347 to 5.1 and 7.0 and hence, Fe−bpydc is much more stable at near-neutral pH. This is a very relevant
348 result because the typical pH of urban wastewater effluents is usually higher than 6.0 (Ganiyu et
349 al., 2018). From the point of view of both, stability and performance, Fe−bpydc can be a
350 promising heterogeneous PEF catalyst for wastewater treatment. Note that TOC detected from
351 the dissolution of organic ligands may compete with bezafibrate and its products to react with
352 •OH, although at pH 5.1 and 7.0 the amount was low (~2.5 mg L^{-1}) and tended to become constant.

353 *3.4. Degradation of micropollutants in urban wastewater*

354 A longer trial was performed to evaluate the mineralization ability of heterogeneous PEF
355 treatment with 0.05 g L^{-1} catalyst, using a BDD/air-diffusion cell at 100 mA in order to enhance
356 the degradation ability of the system. As shown in Fig. S5, TOC was reduced by 61% after 240
357 min of electrolysis, a value much higher than that attained employing other MOFs in non-
358 electrochemical heterogeneous Fenton (Lv et al., 2015). This is feasible from the synergistic
359 oxidation caused by free •OH in the bulk formed and adsorbed BDD(•OH). The residual TOC
360 present in the final solution can be accounted for by the accumulation of refractory oxidation
361 products, like carboxylic acids, and the partial deactivation of Fe−bpydc catalyst.

362 The performance of the (Fe−bpydc) catalyzed PEF system was also evaluated from the
363 treatment of a mixture containing bezafibrate and other micropollutants like bisphenol A,
364 fluoxetine and naproxen, dissolved in conditioned urban wastewater at natural pH 7.2. The
365 concentration decay of each compound is presented in Fig. 6, where 93%, 85% and 78%

degradation can be observed for naproxen, fluoxetine and bisphenol A, respectively, at 90 min. The bezafibrate abatement of 61% was lower than 92% found in 0.050 M Na_2SO_4 solution (Fig. 3). This slower decay can be related to the presence of the other pollutants and natural organic matter, which competitively consumed UV photons and reacted with •OH (Ye et al., 2020a). The lower transparency of the urban wastewater and its higher initial pH are two additional factors that affected negatively to bezafibrate decay. Anyway, these results validate the feasibility of this new heterogeneous PEF treatment.

3.5. Proposed reaction mechanism for heterogeneous PEF and bezafibrate degradation routes

To ascertain the mechanism for (Fe−bpydc)-catalyzed heterogeneous PEF process, ESR analysis was first performed to detect the reactive oxygen species (ROS) generated. The ESR spectra depicted in Fig. S6 exhibit the four typical peaks of DMPO-•OH adduct with an intensity ratio of 1:2:2:1, being an evidence of the dominant role of •OH in this PEF system.

The light absorption and energy band gaps of Fe−bpydc were also ascertained to gain more insight into the reactions involved. Fig. S7a evidences the broad Fe−bpydc adsorption within the UV/Vis region (200-800 nm). The Kubelka-Munk formula was used to convert the data into a Tauc plot (Fig. S7b) to estimate the band gap energy (E_g) of 2.1 eV, according to the procedure by Rao et al. (2014). Valence band XPS (VB-XPS) was recorded to determine the band position of Fe−bpydc. The spectrum of Fig. S7c shows an energy difference of 1.7 eV between the VB energy level (E_{VB}) and the Fermi energy level (E_f). The absolute value of the work function (E_Φ), corresponding to the energy difference between Fermi and vacuum levels, was estimated as 3.7 eV from photoemission spectroscopy (photon energy of 33.2 eV, Fig. S7d) and excitation energy

387 from XPS analysis (29.5 eV). Thus, the VB level (vs vacuum level) was determined as -5.4 eV.
388 Taking into account that 0 V (vs SHE) in the electrochemical potential scale is equivalent to -
389 4.44 eV (vs vacuum level), the latter value corresponded to E_{VB} = 0.96 V as electrochemical
390 energy potential. The conduction band energy E_{CB} (= $E_{VB} - E_g$) was then estimated as -1.14 V.
391 From the aforementioned findings, the catalytic activity mechanism of Fe−bpydc in
392 heterogeneous PEF process is proposed in Fig. 7. The photoinduced electrons (e_{CB}^-) and holes
393 (h_{VB}^+) were generated upon the excitation of Fe−O clusters by UV/Vis illumination, according
394 to photocatalytic reaction (10). In this regard, note that the band diagram suggests that our MOF
395 catalyst behaves as an n-type semiconductor, as the Fermi level lies much closer to the CB. In
396 the absence of H_2O_2 (i.e., UV/Vis photocatalysis), the h_{VB}^+ cannot oxidize H_2O to yield $^\bullet OH$ as
397 the standard oxidation potential of this redox couple (E^0 = 2.73 V vs SHE, Armstrong et al.,
398 2013) is much more positive than the VB value of Fe−bpydc (0.96 V vs SHE). Since it cannot
399 directly oxidize bezafibrate either due to its poor oxidation capacity, the photoinduced carriers
400 recombine very quickly, which justifies the small degree of degradation attained by this process
401 (Fig. 3a). Dissolved O_2 could potentially act as acceptor of e_{CB}^- to form the powerful superoxide
402 radical via reaction (11) (E^0 = -0.18 V, Armstrong et al., 2013, Fig. 7), but this reaction can be
403 neglected based on the poor performance of pure heterogeneous photocatalysis, which is not
404 surprising considering the limited O_2 solubility. This corroborates the absence of $O_2^{\bullet-}$ signals in
405 the ESR analysis (Fig. S6). However, the CB position of Fe−bpydc (-1.14 V vs. SHE) is also
406 more negative (i.e., the e_{CB}^- has enough reduction power) than the reduction potentials of Fe(III)
407 to yield Fe(II) via reaction (12) (E^0 = 0.77 V vs SHE, Guo et al., 2019) and H_2O_2 to yield $^\bullet OH$

via reaction (13) (0.80 V vs SHE, Armstrong et al., 2013). Hence, in heterogeneous PEF process, the recombination of e_{CB}^- and h_{VB}^+ is efficiently prevented thanks to these reactions. On the other hand, Fe(II) at the catalyst surface (≡Fe(II)) reacts with H_2O_2 to form $^{\bullet}OH$ from heterogeneous Fenton's reaction (14) and can be regenerated from the additional ≡Fe(III) reduction via Fenton-like reaction (15), owing to the enhanced electron transfer in the unique 2D MOF structure (Gao et al., 2017). As shown in Fig. 7, H_2O_2 fed in PEF cannot be transformed into superoxide radical by h_{VB}^+ because the E^0 of this couple (1.72 V, Nosaka and Nosaka, 2017) is still much higher than the VB level, which confirms that the main ROS in this heterogeneous PEF process is $^{\bullet}OH$.

$$\text{Fe–bpydc} + h\nu \rightarrow h_{VB}^+ + e_{CB}^- \quad (10)$$

$$O_{2(aq)} + e_{CB}^- \rightarrow O_2^{\bullet-} \quad (11)$$

$$\equiv\text{Fe(III)} + e_{CB}^- \rightarrow \equiv\text{Fe(II)} \quad (12)$$

$$H_2O_2 + e_{CB}^- \rightarrow {}^{\bullet}OH + OH^- \quad (13)$$

$$\equiv\text{Fe(II)} + H_2O_2 \rightarrow {}^{\bullet}OH + \equiv\text{Fe(III)} + OH^- \quad (14)$$

$$\equiv\text{Fe(III)} + H_2O_2 \rightarrow HO_2^{\bullet} + \equiv\text{Fe(II)} + H^+ \quad (15)$$

Fe–bpydc as heterogeneous PEF catalyst shows several advantages over other Fe-based materials: (i) the unique 2D structure leads to easier mass transport; (ii) the greater accessibility of the active sites with H_2O_2 enhances reaction (14) and (15); (iii) the broad light absorption and low band gap energy facilitates the excitation of Fe–O clusters; and (iv) the e_{CB}^- induces additional $^{\bullet}OH$ production and Fe(II) regeneration.

LC-QToF-MS and GC-MS analysis allowed the identification of sixteen main products from bezafibrate degradation, summarized in Table S1 and S2, respectively. Fig. 8 envisages the routes

proposed from the detected derivatives, involving hydroxylation, decarboxylation, dechlorination and C−N bond cleavage. The direct hydroxylation of the aromatic ring of bezafibrate **(1)** with •OH and M(•OH) yielded the monohydroxylated intermediates **2** and **3**, which were subsequently hydroxylated to the polyhydroxylated compounds **4**-**7**. Hydroxylation has also been reported as the preferred reaction pathway in other AOPs (Rivas et al., 2019). The decarboxylation of the lateral group of **1** originated the product **9**, which was then hydroxylated to derivatives **10** and **11**. On the other hand, the hydroxylation on the chlorine position of **1** produced the product **12**, which was further hydroxylated leading compounds **13** and **14**. The decarboxylation of **12** or the dechlorination of **9** yielded the dihydroxylated product **15**. Finally, the cleavage of the C−N bonds present in **1** and on the above derivatives originated the compounds **16** and **8** with a single benzenic ring. Further hydroxylation of **16** yielded **17**.

4. Conclusions

This work demonstrates that it is possible to achieve the quick and complete removal of organic micropollutants like bezafibrate at mild pH using a very small amount (0.05 g L^{-1}) of an Fe−bpydc 2D MOF as heterogeneous UV/Vis PEF catalyst. The numerous active sites of the catalyst enhanced both, mass transport and charge transfer. This allowed an efficient Fenton's reaction continuously sustained with Fe(II), which arouse from surface Fe(III) reduction by photoinduced electrons (e_{CB}^-) and UV/Vis photons. According to the band diagram, the catalyst behaved as an n-type semiconductor, confirming that the photoinduced e_{CB}^- were the major charge carriers. The catalyst underwent a slight deactivation, leading to a performance loss (30%)

after three runs. The stability of Fe−bpydc was much greater at circumneutral pH, showing no evident changes in its crystalline and chemical structure and accumulating small amounts of dissolved iron and TOC. The great potential of (Fe−bpydc)-catalyzed PEF system for industrial application was confirmed from the fast degradation of bezafibrate, bisphenol A, fluoxetine and naproxen in urban wastewater. A thorough reaction mechanism for heterogeneous PEF as well as the bezafibrate degradation routes are finally proposed.

Acknowledgements

The authors thank financial support from project CTQ2016-78616-R (AEI/FEDER, EU), PhD scholarship awarded to Z.H. Ye (State Scholarship Fund, CSC, China) and the Engineering and Physical Sciences Research Council (EPSRC) for funding through the CDT in Advanced Characterization of Materials EP/L015277/1 (G.E.M. Schukraft and C. Petit.) and 2018 NPIF grant EP/S515085/1 (A. L'Hermitte and C. Petit).

References

Alcaide, F., Álvarez, G., Guelfi, D.R.V., Brillas, E., Sirés, I., 2020. A stable CoSP/MWCNTs air-diffusion cathode for the photoelectro-Fenton degradation of organic pollutants at pre-pilot scale. Chem. Eng. J. 379, 122417.

Armstrong, D.A., Huie, R.E., Lymar, S., Koppenol, W.H., Merényi, G., Neta, P., Stanbury, D.M., Steenken, S., Wardman, P., 2013. Standard electrode potentials involving radicals in aqueous solution: inorganic radicals. Bioinorg. React. Mech. 9, 59-61.

468 Bai, W., Li, S., Ma, J., Cao, W., Zheng, J., 2019. Ultrathin 2D metal–organic framework
469 (nanosheets and nanofilms)-based xD–2D hybrid nanostructures as biomimetic enzymes
470 and supercapacitors. J. Mater. Chem. A 7, 9086-9098.
471 Barazesh, J.M., Hennebel, T., Jasper, J.T., Sedlak, D.L., 2015. Modular advanced oxidation
472 process enabled by cathodic hydrogen peroxide production. Environ. Sci. Technol. 49,
473 7391-7399.
474 Barhoumi, N., Oturan, N., Olvera-Vargas, H., Brillas, E., Gadri, A., Ammar, S., Oturan, M.A.,
475 2016. Pyrite as a sustainable catalyst in electro-Fenton process for improving oxidation of
476 sulfamethazine. Kinetics, mechanism and toxicity assessment. Water Res. 94, 52-61.
477 Bello, M.M., Abdul Raman, A.A., Ashgar, A., 2019. A review on approaches for addressing the
478 limitations of Fenton oxidation for recalcitrant wastewater treatment. Process Saf. Environ.
479 Prot. 126, 119-140.
480 Brillas, E., Sirés, I., Oturan, M.A., 2009. Electro-Fenton process and related electrochemical
481 technologies based on Fenton's reaction chemistry. Chem. Rev. 109, 6570-6631.
482 Brunauer, S., Emmett, P.H., Teller, E., 1938. Adsorption of gases in multimolecular layers. J.
483 Am. Chem. Soc. 60, 309-319.
484 Cheng, M., Lai, C., Liu, Y., Zeng, G., Huang, D., Zhang, C., Qin, L., Hu, L., Zhou, C., Xiong,
485 W., 2018. Metal-organic frameworks for highly efficient heterogeneous Fenton-like
486 catalysis. Coord. Chem. Rev. 368, 80-92.

Cornejo, O.M., Murrieta, M.F., Castañeda, L.F., Nava, J.L., 2020. Characterization of the reaction environment in flow reactors fitted with BDD electrodes for use in electrochemical advanced oxidation processes: A critical review. Electrochim. Acta 331, 135373.

Dhakshinamoorthy, A., Asiri, A.M., Garcia, H., 2019. 2D metal-organic frameworks as multifunctional materials in heterogeneous catalysis and electro/photocatalysis. Adv. Mater. 1900617.

Dias, E.M., Petit, C., 2015. Towards the use of metal−organic frameworks for water reuse: a review of the recent advances in the field of organic pollutants removal and degradation and the next steps in the field. J. Mater. Chem. A 3, 22484-22506.

dos Santos, A.J., Sirés, I., Alves, A.P.M., Martínez-Huitle, C.A., Brillas, E., 2020. Vermiculite as heterogeneous catalyst in electrochemical Fenton-based processes: Application to the oxidation of Ponceau SS dye. Chemosphere 240, 124838.

Flores, N., Cabot, P.L., Centellas, F., Garrido, J.A., Rodríguez, R.M., Brillas, E., Sirés, I., 2017. 4-Hydroxyphenylacetic acid oxidation in sulfate and real olive oil mill wastewater by electrochemical advanced processes with a boron-doped diamond anode. J. Hazard. Mater. 321, 566-575.

Finn, R.C., Zubieta, J., 2002. Hydrothermal synthesis and structural characterization of the two-dimensional networks [M(H_2O)(bpy-dicarb)]•H_2O (M=Fe, Co, Ni, Zn; bpy-dicarb=2,2´-bipyridyl-4,4´-dicarboxylic acid). Solid State Sci. 4, 83-86.

Ganiyu, S.O., Zhou, M., Martínez-Huitle, C.A., 2018. Heterogeneous electro-Fenton and photoelectro-Fenton processes: a critical review of fundamental principles and application

for water/wastewater treatment. Appl. Catal. B: Environ. 235, 103-129.

Gao, C., Chen, S., Quan, X., Yu, H., Zhang, Y., 2017. Enhanced Fenton-like catalysis by iron-based metal organic frameworks for degradation of organic pollutants. J. Catal. 356, 125-132.

Guo, T., Wang, K., Zhang, G., Wu, X., 2019. A novel α-Fe_2O_3@g-C_3N_4 catalyst: synthesis derived from Fe-based MOF and its superior photo-Fenton performance. Appl. Surf. Sci. 469, 331-339.

Hinojosa Guerra, M.M., Oller Alberola, I., Malato Rodriguez, S., Agüera López, A., Acevedo Merino, A., Quiroga Alonso, J.M., 2019. Water Res. 156, 232-240.

Hou, X., Hu, K., Zhang, H., Zhang, T., Yang, M., Wang, G., 2019. Construction of 2D MOFs@reduced graphene oxide nanocomposites with enhanced visible light-induced fenton-like catalytic performance by seeded growth strategy. ChemCatChem 11, 4411-4419.

Klidi, N., Clematis, D., Delucchi, M., Gadri, A., Ammar, S., Panizza, M., 2018. Applicability of electrochemical methods to paper mill wastewater for reuse. Anodic oxidation with BDD and $TiRuSnO_2$ anodes. J. Electroanal. Chem. 815, 16-23.

Kondo, A., Noguchi, H., Ohnishi, S., Kajiro, H., Tohdoh, A., Hattori, Y., Xu, W.C., Tanaka, H., Kanoh, H., Kaneko, K., 2006. Novel expansion/shrinkage modulation of 2D layered MOF triggered by clathrate formation with CO_2 molecules. Nano Lett. 6, 2581-2584.

Labiadh, L., Oturan, M.A., Panizza, M., Hamadi, N.B., Ammar, S., 2015. Complete removal of AHPS synthetic dye from water using new electro-fenton oxidation catalyzed by natural

pyrite as heterogeneous catalyst. J. Hazard. Mater. 297, 34-41.

Lanzalaco, S., Sirés, I., Sabatino, M.A., Dispenza, C., Scialdone, O., Galia, A., 2017. Synthesis of polymer nanogels by electro-Fenton process: investigation of the effect of main operation parameters. Electrochim. Acta 246, 812-822.

Le, T.X.H., Esmilaire, R., Drobek, M., Bechelany, M., Vallicari, C., Nguyen, D.L., Julbe, A., Tingry, S., Cretin, M., 2016. Design of a novel fuel cell-Fenton system: a smart approach to zero energy depollution. J. Mater. Chem. A 4, 17686-17693.

Li, W.J., Li, Y., Ning, D., Liu, Q., Chang, L., Ruan, W., 2018. An Fe(II) metal-organic framework as a visible responsive photo-Fenton catalyst for the degradation of organophosphates. New J. Chem. 42, 29-33.

Li, Y., Liu, H., Li, W.J., Zhao, F.Y., Ruan, W.J., 2016. A nanoscale Fe(II) metal-organic framework with a bipyridinedicarboxylate ligand as a high performance heterogeneous Fenton catalyst. RSC Adv. 6, 6756-6760.

Li, X., Wang, B., Cao, Y., Zhao, S., Wang, H., Feng, X., Zhou, J., Ma, X., 2019. Water contaminant elimination based on metal–organic frameworks and perspective on their industrial applications. ACS Sustain. Chem. Eng. 7, 4548-4563.

Liu, C., Wang, Y., Zhang, Y., Li, R., Meng, W., Song, Z., Qi, F., Xu, B., Chu, W., Yuan, D., Yu, B., 2018. Enhancement of Fe@porous carbon to be an efficient mediator for peroxymonosulfate activation for oxidation of organic contaminants: Incorporation NH_2-group into structure of its MOF precursor. Chem. Eng. J. 354, 835-848.

Liu, K., Yu, M., Wang, H., Wang, J., Liu, W., Hoffmann, M.R., 2019. Multiphase porous

electrochemical catalysts derived from iron-based metal−organic framework compounds. Environ. Sci. Technol. 53, 6474-6482.

Ltaïef, A.H., Sabatino, S., Proietto, F., Ammar, S., Gadri, A., Galia, A., Scialdone, O., 2018. Electrochemical treatment of aqueous solutions of organic pollutants by electro-Fenton with natural heterogeneous catalysts under pressure using Ti/IrO_2-Ta_2O_5 or BDD anodes. Chemosphere 202, 111-118.

Lu, J.-Y., Yuan, Y.-R., Hu, X., Liu, W.-J., Li, C.-X., Liu, H.-Q., Li, W.-W., 2020. MOF-derived Fe_2O_3/Nitrogen/Carbon composite as a stable heterogeneous electro-Fenton catalyst. Ind. Eng. Chem. Res. 59, 1800-1808.

Lv, H., Zhao, H., Cao, T., Qian, L., Wang, Y., Zhao, G., 2015. Efficient degradation of high concentration azo-dye wastewater by heterogeneous Fenton process with iron-based metal-organic framework. J. Mol. Catal. A: Chem. 400, 81-89.

Martínez-Huitle, C.A., Rodrigo, M.A., Sirés, I., Scialdone, O., 2015. Single and coupled electrochemical processes and reactors for the abatement of organic water pollutants: a critical review. Chem. Rev. 115, 13362-13407.

Mook, W.T., Aroua, M.K., Issabayeva, G., 2014. Prospective applications of renewable energy based electrochemical systems in wastewater treatment: A review. Renew. Sustain. Ener. Rev. 38, 36-46.

Nosaka, Y., Nosaka, A.Y., 2017. Generation and detection of reactive oxygen species in photocatalysis. Chem. Rev. 117, 11302-11336.

Pérez, T., Coria, G., Sirés, I., Nava, J.L., Uribe, A.R., 2018. Electrosynthesis of hydrogen

peroxide in a filter-press flow cell using graphite felt as air-diffusion cathode. J. Electroanal. Chem. 812, 54-58.

Poza-Nogueiras, V., Rosales, E., Pazos, M., Sanromán. M.A., 2018. Current advances and trends in electro-Fenton process using heterogeneous catalysts – A review. Chemosphere 201, 399-416.

Rao, P.C., S, A.K., Mandal, S., 2014. Synthesis, structure and band gap energy of a series of thermostable alkaline earth metal based metal–organic frameworks. CrystEngComm. 16, 9320-9325.

Rivas, F.J., Solís, R.R., Beltrán, F.J., Gimeno, O., 2019. Sunlight driven photolytic ozonation as an advanced oxidation process in the oxidation of bezafibrate, cotinine and iopamidol. Water Res. 151, 226-242.

Salmerón, I., Plakas, K.V., Sirés, I., Oller, I., Maldonado, M.I., Karabelas, A.J., Malato, S, 2019. Optimization of electrocatalytic H_2O_2 production at pilot plant scale for solar-assisted water treatment. Appl. Catal. B: Environ. 242, 327-336.

Sharma, V.K., Feng, M., 2019. Water depollution using metal-organic frameworks-catalyzed advanced oxidation processes: a review. J. Hazard. Mater. 372, 3-16.

Silva, P., Vilela, S.M.F., Tome, J.P.C., Paz, F.A.A., 2015. Multifunctional metal–organic frameworks: from academia to industrial applications. Chem. Soc. Rev. 44, 6774-6803.

Solís, R.R., Rivas, F.J., Chávez, A.M., Dionysiou, D.D., 2019. Simulated solar photo-assisted decomposition of peroxymonosulfate. Radiation filtering and operational variables influence on the oxidation of aqueous bezafibrate. Water Res. 162, 383-393.

592 Steter, J.R., Brillas, E., Sirés, I., 2018. Solar photoelectro-Fenton treatment of a mixture of
593 parabens spiked into secondary treated wastewater effluent at low input current. Appl. Catal.
594 B: Environ. 224, 410-418.
595 Sui, Q., Gebhardt, W., Schroder, H.F., Zhao, W., Lu, S., Yu, G., 2017. Identification of new
596 oxidation products of bezafibrate for better understanding of its toxicity evolution and
597 oxidation mechanisms during ozonation. Environ. Sci. Technol. 51, 2262-2270.
598 Tang, J., Wang, J., 2018. Metal organic framework with coordinatively unsaturated sites as
599 efficient Fenton-like catalyst for enhanced degradation of sulfamethazine. Environ. Sci.
600 Technol. 52, 5367-5377.
601 Tao, Y., Brigante, M., Zhang, H., Mailhot, G., 2019. Phenanthrene degradation using Fe(III)-
602 EDDS photoactivation under simulated solar light: A model for soil washing effluent
603 treatment. Chemosphere 236, 124366.
604 Taylor, J.M., Vaidhyanathan, R., Iremonger, S.S., Shimizu, G.K.H., 2012. Enhancing water
605 stability of metal-organic frameworks via phosphonate monoester linkers. J. Am. Chem.
606 Soc. 134, 14338-14340.
607 Thommes, M., Kaneko, K., Neimark, A.V., Olivier, J.P., Rodriguez-Reinoso, F., Rouquerol, J.,
608 Sing, K.S.W., 2015. Physisorption of gases, with special reference to the evaluation of
609 surface area and pore size distribution, IUPAC Technical Report, 87(9-10), 1051-1069.
610 Welcher, F.J., 1975. Standard Methods of Chemical Analysis, sixth ed, vol. 2, R.E. Krieger
611 Publishing Co, Huntington, New York, Part B.
612 Yang, W., Zhou, M., Oturan, N., Li, Y., Oturan, M.A, 2019. Electrocatalytic destruction of

pharmaceutical imatinib by electro-Fenton process with graphene-based cathode. Electrochim. Acta 305, 285-294.

Ye, Z., Brillas, E., Centellas, F., Cabot, P.L., Sirés, I., 2019. Electro-Fenton process at mild pH using Fe(III)-EDDS as soluble catalyst and carbon felt as cathode. Appl. Catal. B: Environ. 257, 117907.

Ye, Z., Brillas, E., Centellas, F., Cabot, P.L., Sirés, I., 2020a. Expanding the application of photoelectro-Fenton treatment to urban wastewater using the Fe(III)-EDDS complex. Water Res. 169, 115219.

Ye, Z., Padilla, J.A., Xuriguera, E., Beltran, J.L., Alcaide, F., Brillas, E., Sirés, I., 2020b. A highly stable metal-organic framework-engineered FeS_2/C nanocatalyst for heterogeneous electro-Fenton treatment: Validation in wastewater at mild pH. Environ. Sci. Technol. 54, 4664-4674.

Ye, Z., Padilla, J.A., Xuriguera, E., Brillas, E., Sirés, I., 2020c. Magnetic MIL(Fe)-type MOF-derived N-doped nano-ZVI@C rods as heterogeneous catalyst for the electro-Fenton degradation of gemfibrozil in a complex aqueous matrix. Appl. Catal. B: Environ. 266, 118604.

Yin, Z., Tian, Y., Gao, P., Feng, L., Liu, Y., Du, Z., Zhang, L., 2020. Photodegradation mechanism and genetic toxicity of bezafibrate by Pd/g-C_3N_4 catalysts under simulated solar light irradiation: the role of active species. Chem. Eng. J. 379, 122294.

Zhang, Q., Zhou, M., Ren, G., Li, Y., Li, Y., Du, X., 2020. Highly efficient electrosynthesis of hydrogen peroxide on a superhydrophobic three-phase interface by natural air diffusion.

634 Nat. Comm. 11, 1731.
635 Zhao, H., Chen, Y., Peng, Q., Wang, Q., Zhao, G., 2017. Catalytic activity of
636 MOF(2Fe/Co)/carbon aerogel for improving H_2O_2 and $^{\bullet}OH$ generation in solar photo–
637 electro–Fenton process. Appl. Catal. B: Environ. 203, 127-137.
638 Zhou, M., Oturan, M.A., Sirés, I. (Eds.), 2018. Electro-Fenton Process: New Trends and Scale-
639 Up. Springer Nature, Singapore.
640 Zhou, W., Meng, X., Gao, J., Alshawabkeh, A.N., 2019. Hydrogen peroxide generation from O_2
641 electroreduction for environmental remediation: A state-of-the-art review. Chemosphere
642 225, 588-607.
643 Zhu, Y., Zhu, R., Xi, Y., Xu, T., Yan, L., Zhu, J., Zhu, G., He, H., 2018. Heterogeneous photo-
644 Fenton degradation of bisphenol A over Ag/AgCl/ferrihydrite catalysts under visible light.
645 Chem. Eng. J. 346, 567-577.

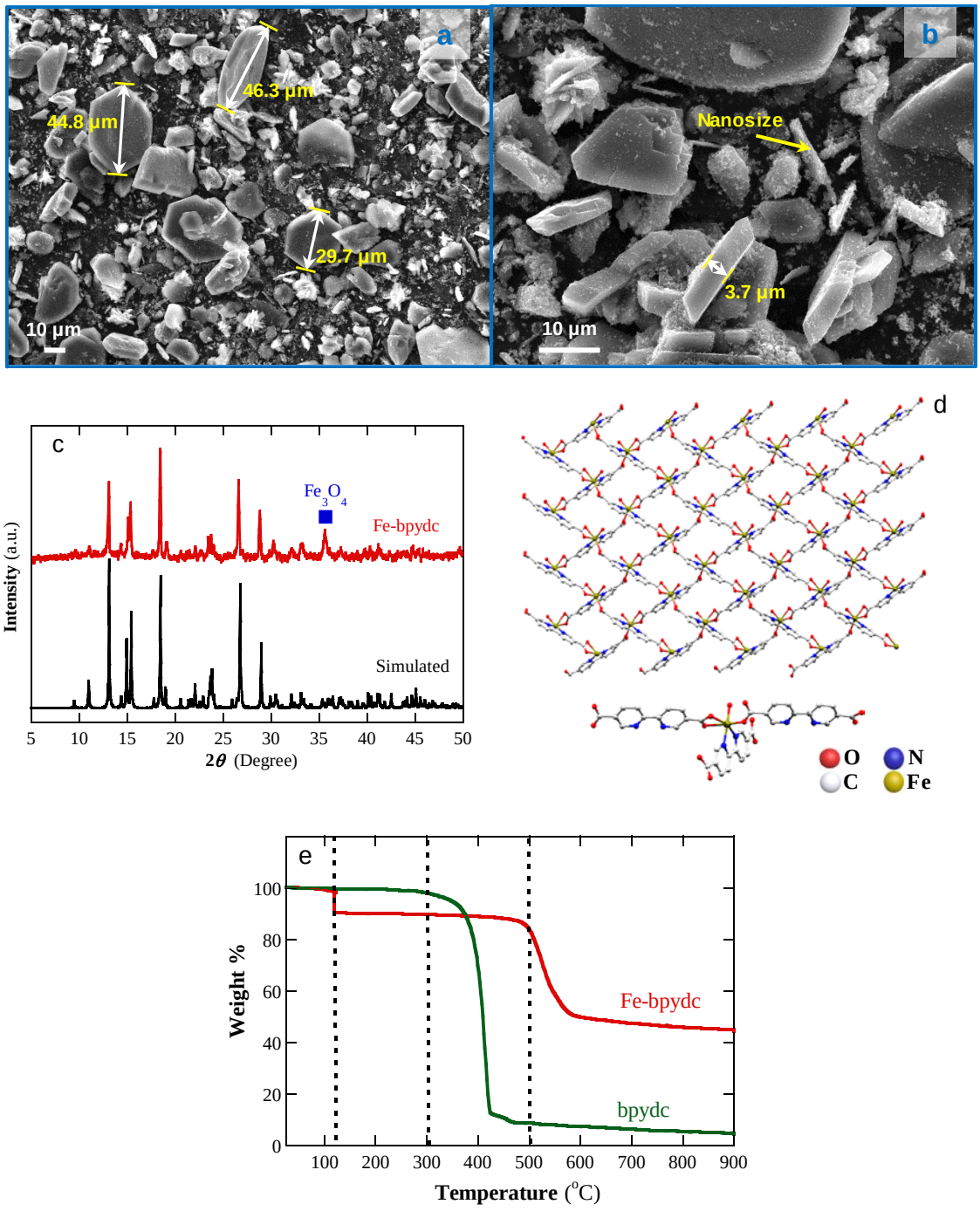

Fig. 1. FESEM images at (a) 500× and (b) 1,000×, (c) XRD patterns, (d) pictorial representation of the structure of the as-synthesized Fe−bpydc (lattice waters are omitted for clarity) and (e) thermogravimetric analysis.

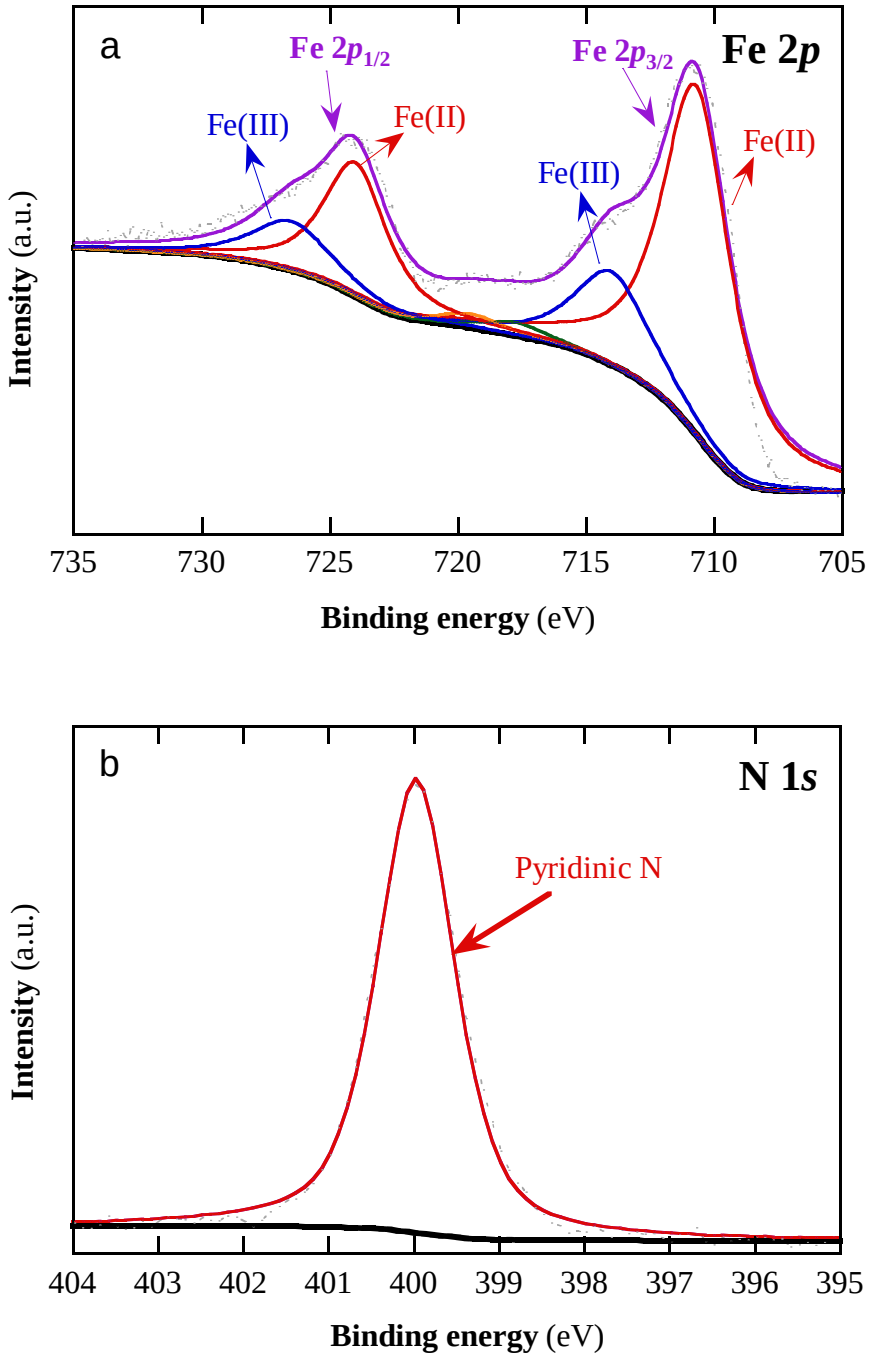

Fig. 2. XPS core level spectra of the Fe−bpydc catalyst: (a) Fe 2*p* and (b) N 1*s*.

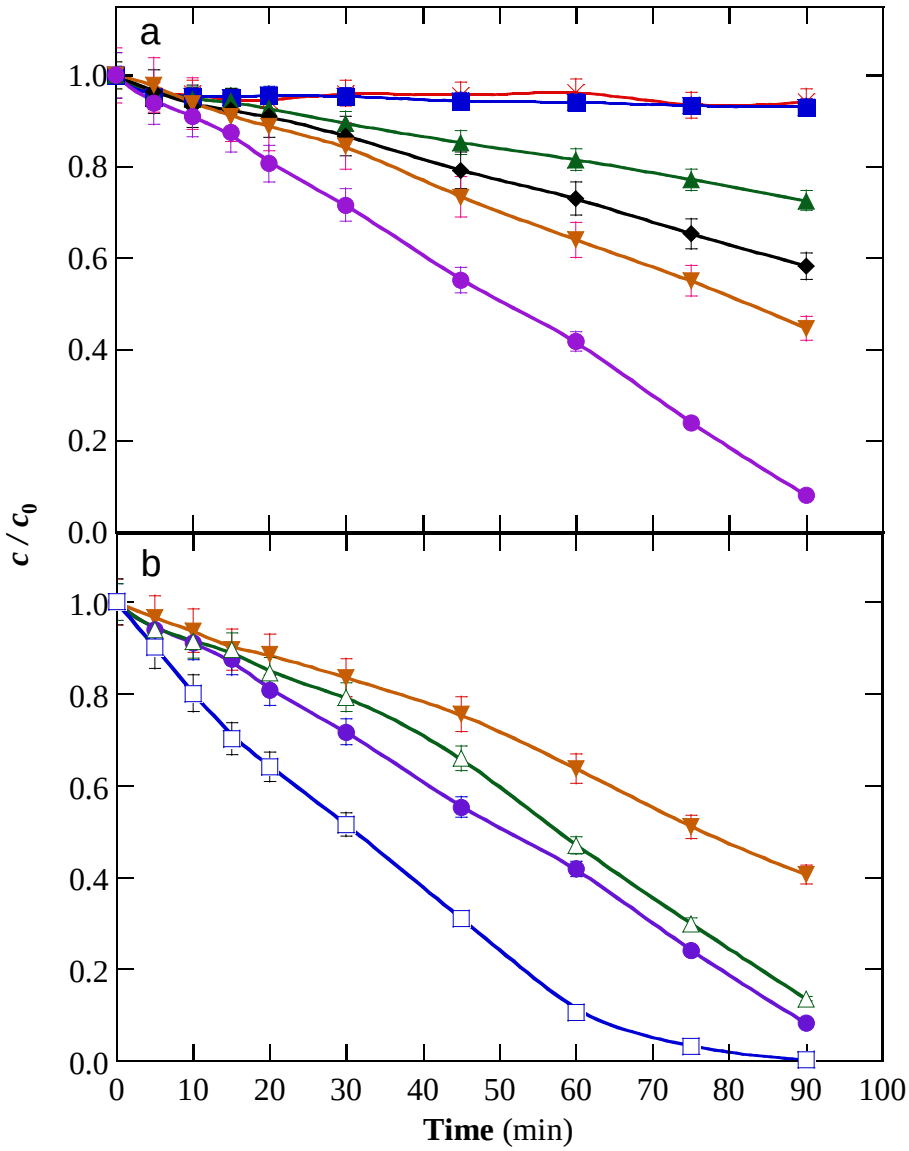

Fig. 3. Normalized bezafibrate concentration decay during different treatments of 150 mL of 0.044 mM (10 mg C L^{-1}) drug solutions with 0.050 M Na_2SO_4 at natural pH ~ 5.1. In the electrochemical assays, an IrO_2/air-diffusion cell was used, at 100 mA and 25 ºC. In (a), (×) adsorption trials with 0.05 g L^{-1} Fe−bpydc, (■) UV/Vis photocatalysis with 0.05 g L^{-1} Fe−bpydc, (▲) EO-H_2O_2, (◆) EF with 0.05 g L^{-1} Fe−bpydc, (▼) visible-light PEF with 0.05 g L^{-1} Fe−bpydc and (●) UV/Vis PEF with 0.05 g L^{-1} Fe−bpydc. In (b), (△) visible-light PEF and (□) UV/Vis PEF, both with 0.05 g L^{-1} Fe−bpydc. A Xe lamp of 150 W and 300 W was employed in the photoassisted treatments of plot (a) and (b), respectively.

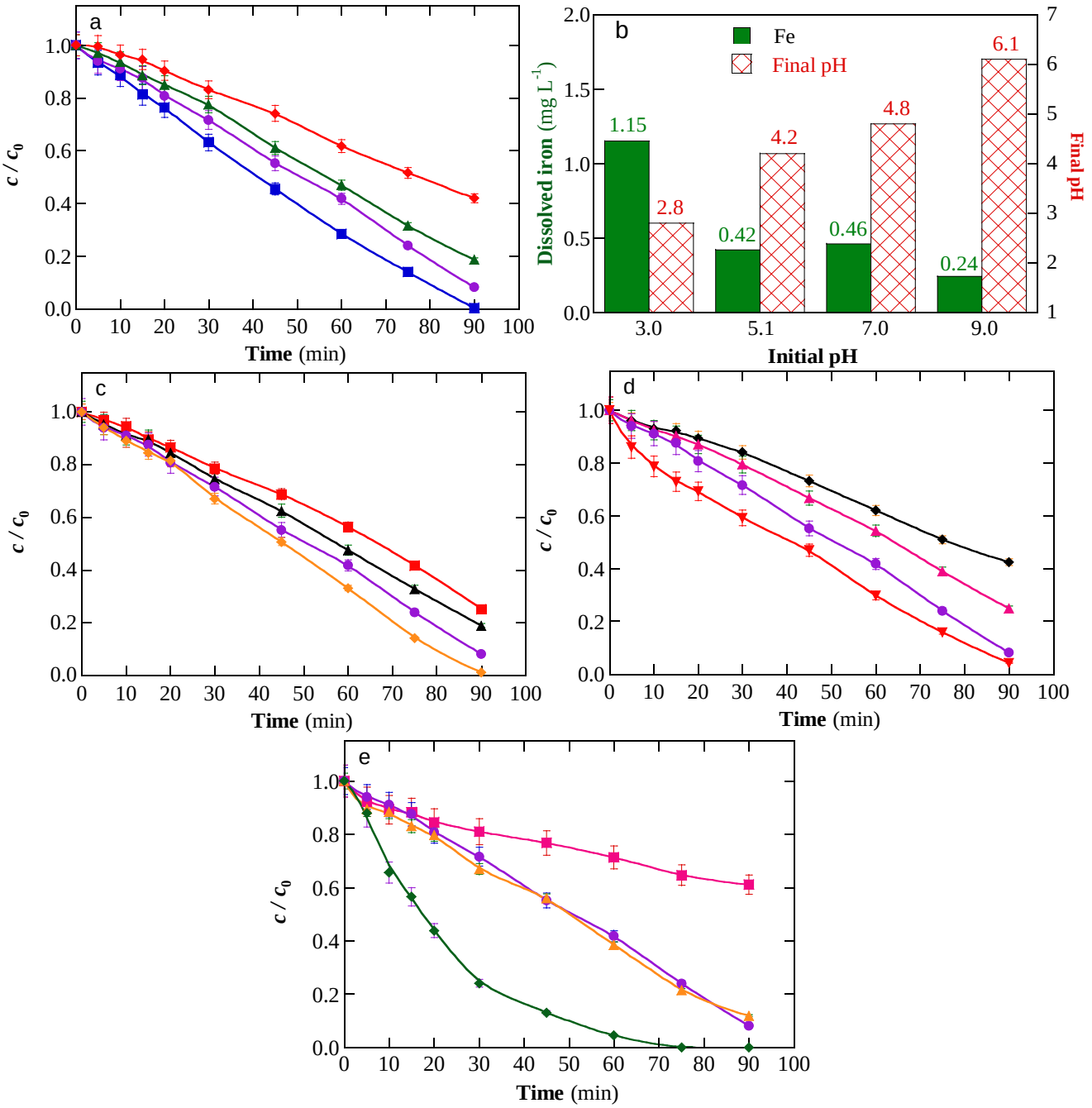

Fig. 4. (a,c,d,e) Time course of normalized bezafibrate concentration during the heterogeneous UV/Vis PEF treatments of 150 mL of 0.044 mM drug solutions with 0.050 M Na_2SO_4, using an IrO_2/air-diffusion cell (except in plot e) with Fe−bpydc catalyst at 25 ºC under irradiation with a 150 W Xe lamp. (b) Iron concentration (filled bar) and final pH (dashed bar) after 90 min of the trials of plot (a). In (a), 0.05 g L^{-1} catalyst, at 100 mA and different initial pH: (■) 3.0, (●) 5.1, (▲) 7.0 and (◆) 9.0. In (c), pH 5.1 and 0.05 g L^{-1} catalyst, at different applied current values: (■) 50, (▲) 75, (●) 100 and (◆) 150 mA. In (d), pH 5.1 and 100 mA, at different catalyst doses: (◆) 0.0125, (▲) 0.025, (●) 0.05 and (▼) 0.075 g L^{-1} Fe−bpydc. In (e), effect of anode and electrolyte at its natural pH, with 0.05 g L^{-1} catalyst at 100 mA, using: (■) IrO_2-based anode, in 0.041 M Na_2SO_4 + 0.009 M $NaHCO_3$ solution, (▲) BDD anode, in 0.050 M Na_2SO_4 solution, (●) IrO_2-based anode, in 0.050 M Na_2SO_4 solution and (◆) RuO_2-based anode, in 0.025 M Na_2SO_4 + 0.035 M NaCl solution.

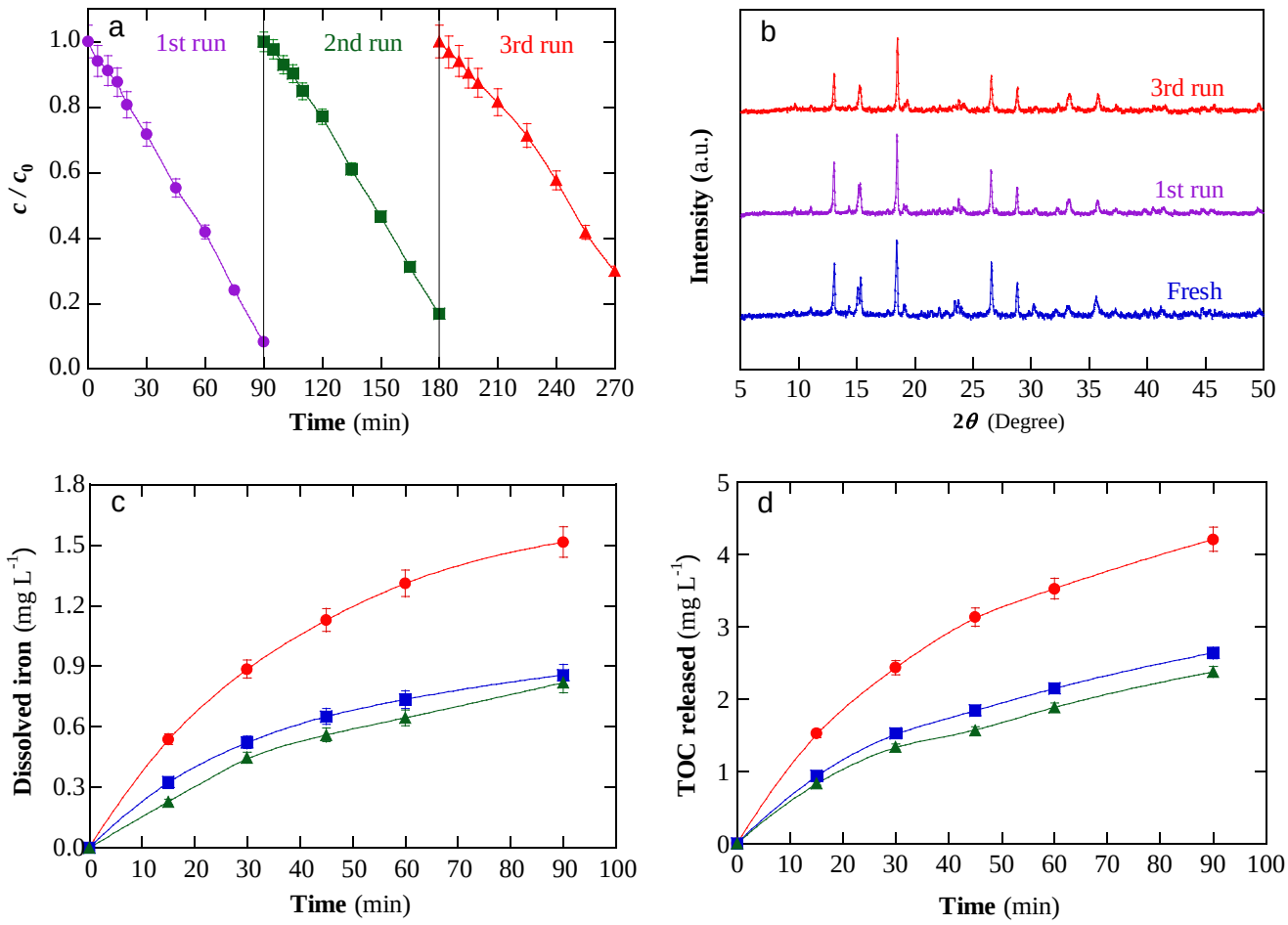

Fig. 5. (a) Reusability of Fe−bpydc in three consecutive runs of heterogeneous UV/Vis PEF treatment with 0.05 g L^{-1} catalyst (see description in Fig. 3a). (b) XRD pattern of fresh and used Fe−bpydc. Time course of concentration of (c) dissolved iron and (d) TOC, released during constant stirring of 0.05 g L^{-1} Fe−bpydc in Milli-Q water at initial pH of: (●) 3.0, (■) 5.1 and (▲) 7.0.

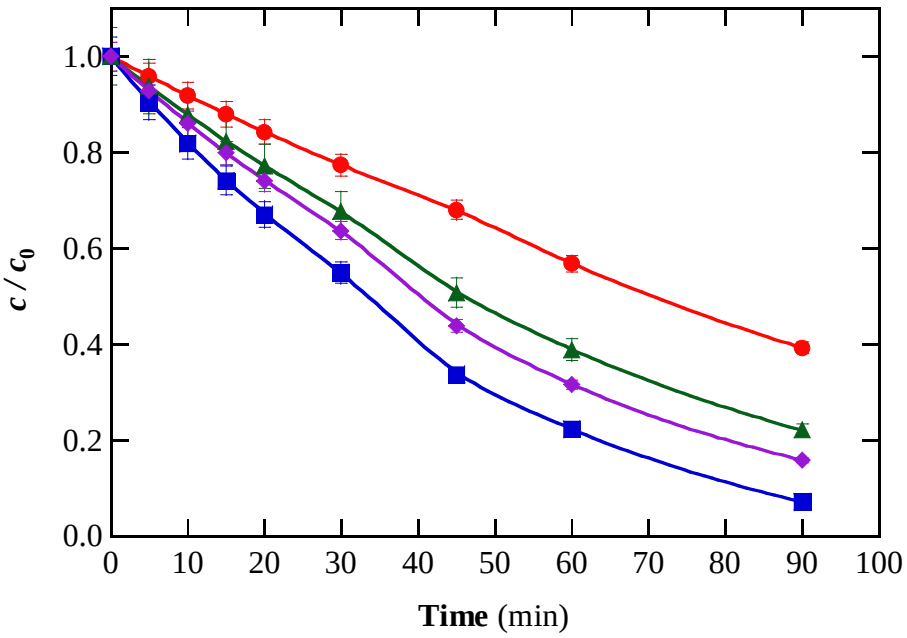

Fig. 6. Degradation of four selected micropollutants (each at a concentration of 10 mg C L^{-1}), spiked together into 150 mL of urban wastewater at natural pH 7.4, by heterogeneous UV/Vis PEF treatment with 0.05 g L^{-1} Fe−bpydc using an IrO_2/air-diffusion cell at 100 mA and 25 ºC under irradiation with a 150 W Xe lamp. Micropollutants: (●) Bezafibrate, (▲) bisphenol A, (◆) fluoxetine and (■) naproxen.

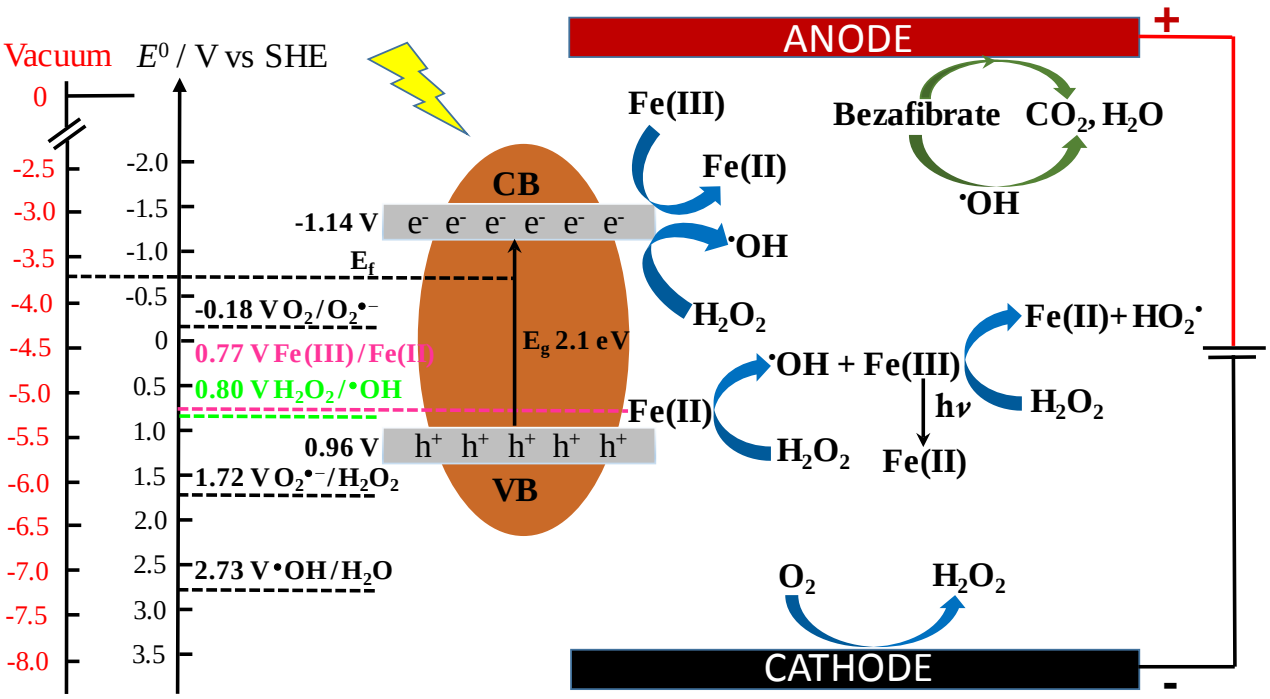

Fig. 7. Proposed mechanism for (Fe−bpydc)-catalyzed heterogeneous PEF treatment at mild pH.

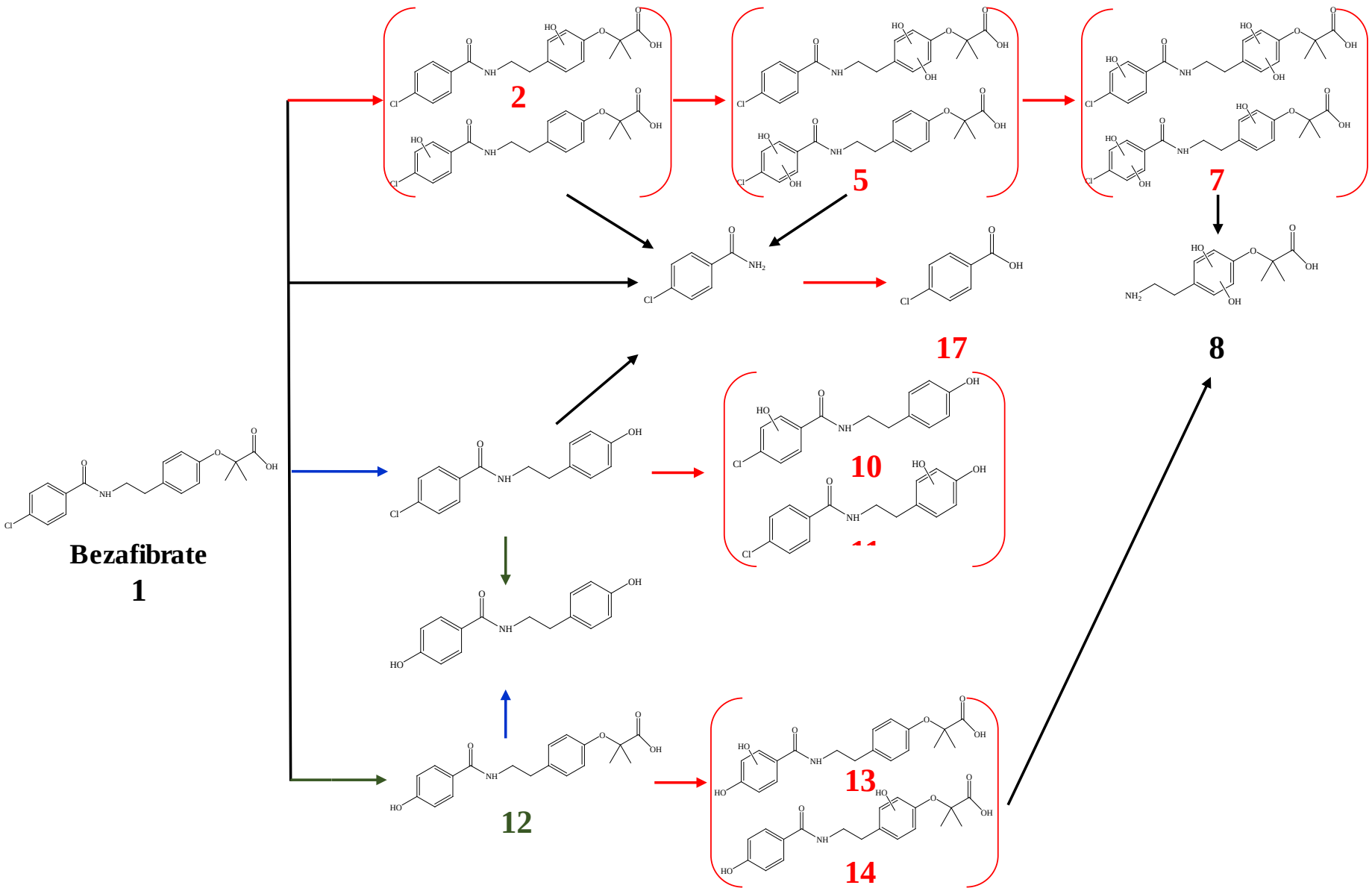

Fig. 8. Degradation routes proposed for bezafibrate degradation by (Fe−bpydc)-catalyzed PEF treatment at mild pH.